THE JOURNAL OF BIOLOGICAL CHEMISTRY VOL. 283, NO. 38, pp. 26241–26251, September 19, 2008

Molecular Shape, Architecture, and Size of $P2X_4$ Receptors Determined Using Fluorescence Resonance Energy Transfer and Electron Microscopy*

Received for publication, June 10, 2008, and in revised form, July 14, 2008 Published, JBC Papers in Press, July 17, 2008, DOI 10.1074/jbc.M804458200

Mark T. Young[‡1], **James A. Fisher**[§], **Samuel J. Fountain**[¶], **Robert C. Ford**[‡], **R. Alan North**[¶], **and Baljit S. Khakh**[§‖2]

From the [‡]*Manchester Interdisciplinary Biocentre, University of Manchester, Manchester M1 7DN, United Kingdom, the* [§]*Medical Research Council Laboratory of Molecular Biology, Cambridge CB2 0QH, United Kingdom, the* [¶]*Faculty of Life Sciences, University of Manchester, Manchester M13 9PT, United Kingdom, and the* [‖]*Departments of Physiology and Neurobiology, David Geffen School of Medicine, UCLA, Los Angeles, California 90095-1751*

P2X receptors are ATP-gated nonselective cation channels with important physiological roles. However, their structures are poorly understood. Here, we analyzed the architecture of P2X receptors using fluorescence resonance energy transfer (FRET) microscopy and direct structure determination using electron microscopy. FRET efficiency measurements indicated that the distance between the C-terminal tails of $P2X_4$ receptors was 5.6 nm. Single particle analysis of purified $P2X_4$ receptors was used to determine the three-dimensional structure at a resolution of 21 Å; the orientation of the particle with respect to the membrane was assigned by labeling the intracellular C termini with 1.8-nm gold particles and the carbohydrate-rich ectodomain with lectin. We found that human $P2X_4$ is a globular torpedo-like molecule with an approximate volume of 270 nm^3 and a compact propeller-shaped ectodomain. In this structure, the distance between the centers of the gold particles was 6.1 nm, which closely matches FRET data. Thus, our data provide the first views of the architecture, shape, and size of single P2X receptors, furthering our understanding of this important family of ligand-gated ion channels.

P2X receptors, of which seven subtypes are found in mammals, display a diverse tissue distribution and play key roles in a variety of physiological processes such as neurotransmission, sensory transduction, inflammation, and cardiovascular regulation (1–3). They are found mostly on the plasma membrane, but in some species such as *Dictyostelium* may also fulfill physiological functions within intracellular membranes (4). They are the third major superfamily of ligand-gated ion channels; however, in contrast to other cationic channel superfamilies (5–7), very little is known about their three-dimensional structure.

The topology of P2X receptors is well defined; each monomer subunit is predicted to possess intracellular N and C termini, two transmembrane-spanning domains, and a large ectodomain (2). The functional channel unit is thought to be a trimer (8–11), a feature that is shared with acid-sensing ion channels (12). A low resolution structural study of the rat $P2X_2$ isoform has been published; electron microscopy of single particles gave rise to a structure with a volume of ~1200 nm^3 (13). However, the orientation of the molecule was not assigned, and there was no independent evidence to verify the dimensions. Moreover, atomic force microscopy (AFM)[3] studies suggest a smaller molecular volume of 490 nm^3; however, these studies modeled the channel as a flat spherical cap with a height of 2.9 nm (10, 14). Because the thickness of the plasma membrane is ~7 nm, this implies that the AFM studies reported on molecules in a squashed conformation (10, 14). Thus, the available data do not provide a consistent or satisfying view of the shape, architecture, or size of P2X receptors.

To further our structural knowledge of P2X receptors and to address the above discrepancies in estimates of molecular volume and size, we have explored two parallel experimental approaches. First, we measured the efficiency of fluorescence resonance energy transfer (FRET) between subunits within homomeric P2X receptors bearing yellow (YFP) or cyan (CFP) fluorescent protein tags at their C termini. Extensive previous studies by us and others have employed green fluorescent protein (GFP)-labeled P2X receptors (15–25), demonstrating that tagging $P2X_2$, $P2X_4$, and $P2X_5$ receptors on the C termini with GFP does not affect receptor function. Second, we overexpressed $P2X_4$ in human embryonic kidney 293 (HEK293) cells and purified the trimeric form to homogeneity. We used single particle analysis and domain-specific labeling to generate the three-dimensional structure of human $P2X_4$ at a resolution of 21 Å, oriented with respect to the lipid bilayer.

* This work was supported, in whole or in part, by the National Institutes of Health (to B. S. K., subcontract on Grant GM070925). This work was also supported by the Wellcome Trust (to R. A. N.), the Medical Research Council (to J. A. F. and B. S. K.), and the Human Frontier Science Program (to B. S. K.). The costs of publication of this article were defrayed in part by the payment of page charges. This article must therefore be hereby marked "*advertisement*" in accordance with 18 U.S.C. Section 1734 solely to indicate this fact.

⌘ *Author's Choice*—Final version full access.

[1] Recipient of a Wellcome Trust advanced training fellowship.

[2] To whom correspondence should be addressed: Depts. of Physiology and Neurobiology, David Geffen School of Medicine, UCLA, 10833 Le Conte Ave., Los Angeles, CA 90095-1751. E-mail: bkhakh@mednet.ucla.edu.

[3] The abbreviations used are: AFM, atomic force microscopy; FRET, fluorescence resonance energy transfer; YFP, yellow fluorescent protein; CFP, cyan fluorescent protein; GFP, green fluorescent protein; HEK293, human embryonic kidney 293; DDM, β-D-dodecyl maltoside; PFO, perfluorooctanoic acid; Ni-NTA, nickel-nitrilotriacetic acid; EM, electron microscopy.

EXPERIMENTAL PROCEDURES

Molecular and Cell Biology—HEK293 or HEK293T cells transiently expressing the appropriate wild-type and fluorescently labeled P2X receptor subunits were used. Some cDNAs were available from previous work (18–20), and others were generated using standard cloning procedures. The resulting plasmids were verified by sequencing ($P2X_1$–$P2X_7$, all tagged with either CFP or YFP). The plasmids were propagated in *Escherichia coli* DH5α. The plasmid encoding human $P2X_4$ with a C-terminal EYMPME tag has been described previously (26). Human $P2X_4$ containing a C-terminal decahistidine tag was generated from this construct by PCR. HEK293 cells (obtained from American Type Culture Collection) were maintained in 75-cm^2 cell culture flasks (Corning) in Dulbecco's modified Eagle's medium/nutrient mixture F-12 with Glutamax (Invitrogen) supplemented with 10% fetal bovine serum and penicillin/streptomycin. Cells were grown in a humidified atmosphere of 95% air and 5% CO_2 at 37 °C in a cell culture incubator. The cells were split 1 in 10 when confluence reached 60–90%, which was generally every 4 days. Cells were prepared for transfection by plating onto 6-well plates at the time of splitting, 3–4 days before transfection. They were transfected at ~60% confluence. For transient expression in HEK293 cells, we used 0.5–1 μg of plasmid cDNA and Effectene transfection reagent (Qiagen Inc.) for each well of a 6-well plate. The manufacturer's instructions were followed, with 4 μl of enhancer and 10 μl of Effectene were used for each transfection. The transfection efficiency was 40–60%. The HEK293 stable cell line constitutively expressing human $P2X_4$-His_{10} was generated using electroporation and selection with 400 μg/ml G418 (Invitrogen, Paisley, UK) for 14 days in 15-cm culture dishes. Single colonies were isolated using sterile greased stainless steel rings, trypsin-treated, and transferred to 24-well plates. Expression of $P2X_4$-His_{10} was verified by Western blotting according to standard protocols, and the highest expressing clone was selected for overexpression.

Epifluorescence FRET Microscopy—We have previously described the setup (19). We used an Olympus BX50 microscope equipped with a Peltier cooled (−15 °C) Imago CCD camera (640 × 480 pixels, each pixel 9.9 × 9.9 μm), epifluorescence condenser, control unit (containing ISC and PDC boards), and a Polychrome IV monochromator (all from Till Photonics). The light from the monochromator was led to the microscope through a quartz fiber light guide. The hardware was controlled by a personal computer, an appropriate frame grabber (TILL Photonics), and macros driven by TILLvisION Version 3.3 software. The cells were viewed with a 40× water immersion objective lens with a numerical aperture of 0.8 (Olympus). We used the following filters for acquiring CFP or YFP images (all from Glen Spectra, Stanmore, UK; order is dichroic, emitter in nanometers): CFP (455DRLP, 480AF30) and YFP (525DRLP, 545AF35). To photodestroy the YFP, we used 525 nm light from the monochromator and a 525DRLP dichroic.

Electrophysiology—HEK293 cells were used for recordings 24–48 h post-transfection. Cells were gently mechanically dispersed and plated onto glass coverslips 2–12 h before use. We included this step (27) to ensure adequate voltage clamp during reversal potential measurements from single spherical cells. The extracellular recording solution comprised 150 mM NaCl, 1 mM $MgCl_2$, 1 (or 0.1) mM $CaCl_2$, 10 mM HEPES, and 10 mM glucose (pH 7.4), and the pipette solution comprised 154 mM NaCl (or CsCl or CsF), 11 mM EGTA, and 10 mM HEPES. Whole-cell voltage-clamp recordings were made with ~4-megaohm borosilicate glass electrodes (World Precision Instruments) using an Axopatch-1D or Axopatch 200 amplifier controlled by a computer running pCLAMP 8.1 or 10 software via a Digidata 1322 interface (Molecular Devices). Data were filtered at 0.5–2 kHz and digitized at 1–5 kHz. Drugs were applied to single cells by pressure ejection using a Picospritzer (Intracell Ltd.) or in the bathing medium, which flowed at 2–3 ml/min. For pressure application (~20 p.s.i., 1 p.s.i. = 6.89 kilopascals), we used 2–4-megaohm pipettes as described previously (21); solution exchange occurred in ~10 ms.

Protein Purification—Membrane fractions were prepared from 2.5×10^8 cells and solubilized in phosphate-buffered saline containing 1% (w/v) β-D-dodecyl maltoside (DDM; Merck, Nottingham, UK) and protease inhibitors (Complete-EDTA, Roche Applied Science). Samples were diluted into buffer A (150 mM NaCl, 20 mM sodium phosphate (pH 7.4), 150 mM imidazole, and 0.1% (w/v) DDM) and incubated overnight at 4 °C with nickel-Sepharose beads (Amersham Biosciences, Chalfont St. Giles, UK) to capture His-tagged protein. Beads were packed into columns and washed with 20 column volumes of buffer A; 50% pure His-tagged protein was eluted in buffer A containing 500 mM imidazole.

Purification of $P2X_4$ Trimers—1-ml protein-containing fractions from the nickel affinity column were concentrated using 50-kDa cutoff filters (Millipore, Watford, UK) and separated by perfluorooctanoic acid (PFO)-PAGE according to published methods (28). For preparative PFO-PAGE, samples were loaded onto 1.5-mm thick 8% (w/v) polyacrylamide gels and run at 4 °C at 10 mA. $P2X_4$ trimers (150–180 kDa) were excised from nonstained gels and placed into 2-ml D-tube dialysis units (Merck), and protein was eluted at 60 V for 2 h at 4 °C. Protein samples were diafiltered into phosphate-buffered saline containing 0.1% (w/v) DDM.

Gold and Lectin Labeling—For gold labeling, purified $P2X_4$-His_{10} in 0.1% DDM was incubated for 10 min at room temperature with a 10:1 molar excess of 1.8-nm diameter nickel-nitrilotriacetic acid (Ni-NTA)-Nanogold particles (Nanoprobes, Yaphank, NY). Samples were adsorbed onto grids and washed with Nanogold suspension to prevent unbinding of the protein-associated gold particles. For lectin labeling, purified $P2X_4$-His_{10} in 0.1% DDM was mixed with *Lens culinaris* lectin (Sigma, Poole, UK) at a molar ratio of 1:1 and immediately applied to grids. After transmission electron microscopy and image processing, 1966 gold-labeled $P2X_4$-His_{10} particles (in 48 × 48 pixel boxes) and 2862 lectin-labeled particles (in 64 × 64 pixel boxes) were manually selected. Three-dimensional structures were generated using the refined $P2X_4$ structure as a starting model with eight rounds of iterative refinement.

Structure Determination by Electron Microscopy and Single Particle Analysis—Protein samples (20 μg/ml) were adsorbed onto glow-discharged carbon-coated copper grids and nega-

tively stained with 2% (w/v) uranyl acetate. Transmission electron microscopy images were recorded on Kodak SO-163 film at a calibrated magnification of ×43,500 using a Tecnai 10 electron microscope operating at 100 kV. Images were digitized using a UMAX 2000 Powerlook scanner at 1200 pixels/inch, providing a specimen level increment of 4.87 Å/pixel. EMAN software (29) was used to manually select, filter, and process 6826 particles in 48 × 48 pixel boxes. Using the command "startcsym," we compared the best match of the two-dimensional reference-free class averages with symmetrized classes using C2, C3, C4, C5, and C6 symmetry (see Fig. 3*E*). C3 symmetry provided the best fit to the data, and so a start model was generated from a manually selected set of reference-free class averages with C3 symmetry applied using the command "startAny"; this model was refined by 12 rounds of iterative projection matching using the "refine" command. Fourier shell correlation analysis of the final iteration using comparison of structures generated from even- or odd-numbered particles ("eotest"; see Fig. 3*D*) indicated a final resolution of ~21 Å. Structures were displayed at volume shells corresponding to at least 3 S.D. values above the mean density.

Imaging Data Analysis—For donor dequenching experiments, the FRET efficiency (e) was calculated as $e = (1 - (I_{C\text{-before}}/I_{C\text{-after}})) \times 100$, where $I_{C\text{-before}}$ is the donor fluorescence intensity before photodestruction and $I_{C\text{-after}}$ is the intensity after photodestruction. The photodestruction of the YFP proceeds with kinetics similar to the dequenching of the donor (see Fig. 1*C*), and plotting the photorecovery *versus* photodestruction yields a linear plot (see Fig. 2). We used such linear plots and extrapolated to 100% acceptor photodestruction to calculate the maximum donor dequenching for epifluorescence microscopy: e is given by the y axis intercept. In a specific set of experiments, we also calculated FRET e from just one point of photodestruction and extrapolated to 100% destruction. We did this to ensure that the estimates of e were not affected by the method used to measure FRET (see Fig. 4), particularly for P2X$_1$ and P2X$_7$ receptors (see "Results").

To approximate distances, we used the Förster equation, $e = R_0^6/(R_0^6 + R^6)$, where $R_0^6 = (8.79 \times 10^{23})\kappa^2 n^{-4} \phi_D J_{DA}$, e is the experimentally determined FRET efficiency, and R is the distance between donor and acceptor fluorophores (30, 31). R_0 includes terms for the donor quantum efficiency (ϕ_D), the solvent refractive index (n), overlap of the donor emission and acceptor absorption spectra (J_{DA}), and the orientation factor (κ^2). R_0 is the distance at which e is 50% for any given fluorophore pair. In the case of CFP and YFP, this is ~50 Å (5 nm). Notably, R_0 contains a term for the fluorophore dipole orientation factor (κ^2), which at 2/3 assumes random tumbling of the fluorophores (30). This means that R_0 and the distance measurements reported here assume that the fluorophores adopt all spherically random orientations. Given that we do not know the relative orientation of the fluorophores on P2X$_2$ channels, assuming a κ^2 value of 2/3 seems appropriate (30). When interpreting FRET e measurements in terms of distance, it is important to consider that in the case of CFP and YFP the fluorophore is buried in the center of a β-can with a width of 30 Å and a length of 45 Å (32). A further consideration is that we do not know the absolute ratio of donors to acceptors during FRET at the single molecule level. We have previously considered these issues in depth (18, 19). For the FRET experiments, we chose plasma membrane regions of interest post hoc. Our criteria were that regions of interest (i) were bright in both CFP and YFP images; (ii) located at the edge, presumably plasma membrane of the cell; (iii) did not change or drift in intensity during the control period; and (iv) remained in focus during the entire experiment.

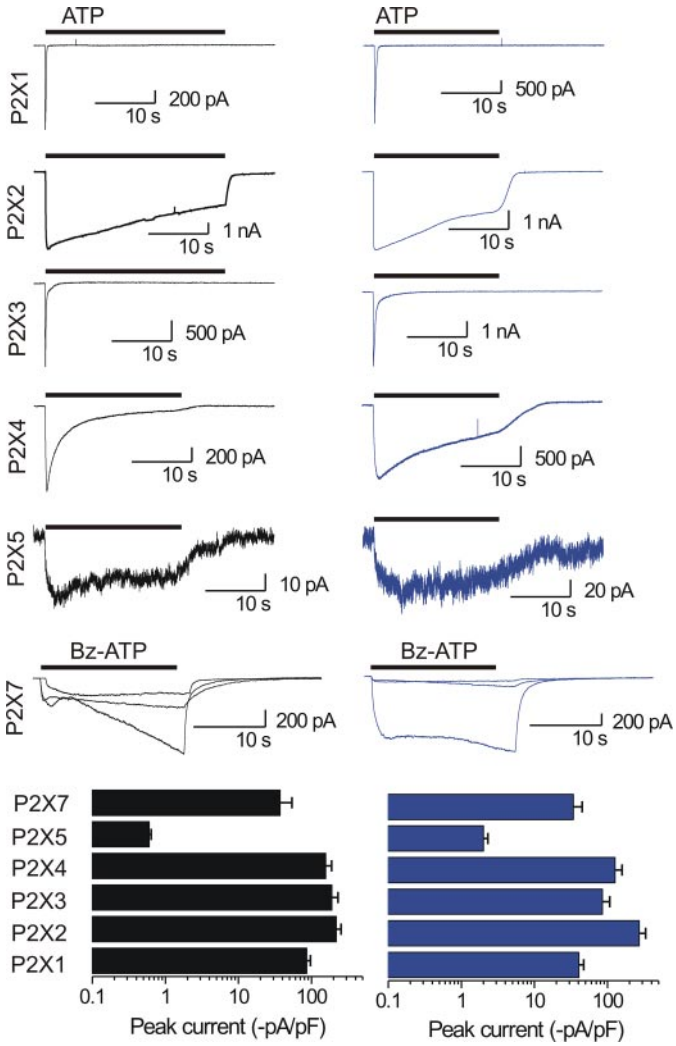

FIGURE 1. **Functional analysis of wild-type and YFP-tagged P2X receptors.** The *black traces* show agonist-evoked currents for wild-type homomeric P2X$_1$–P2X$_5$ and P2X$_7$ receptors. In each case, the agonist was applied for 20–30 s so that the time course of desensitization could be monitored (100 μM ATP for P2X$_1$–P2X$_5$ and 30 μM benzoyl (*Bz*)-ATP for P2X$_7$). The *blue traces* show similar experiments for the same receptors carrying YFP tags. Note that the response is similar for each receptor with or without the tag. The bar graphs below show peak current densities; here again, the peaks for wild-type and YFP-tagged receptors were similar. P2X$_6$ receptors were not examined because they do not express in the plasma membrane. *pF*, picofarads.

RESULTS

Tagged P2X Receptors Are Functional—In past work, it has been demonstrated that P2X$_2$, P2X$_4$, and P2X$_5$ receptors tagged on their C termini with GFP function like their wild-type counterparts in terms of ATP-evoked currents and ATP sensitivity (15–25). We started by recording ATP-evoked currents from HEK cells expressing CFP- and YFP-tagged P2X receptors and

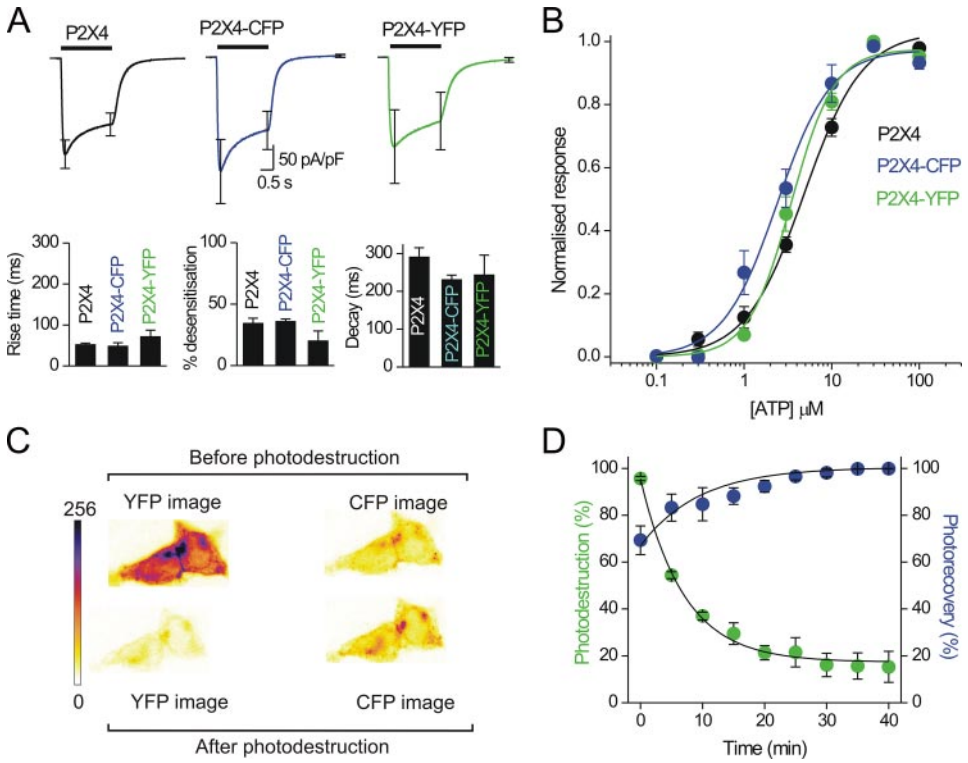

FIGURE 2. **Functional properties and FRET for CFP- and YFP-tagged P2X$_4$ receptors.** *A*, average 100 μM ATP-evoked current traces for P2X$_4$, P2X$_4$-CFP, and P2X$_4$-YFP receptors ($n = 9$), with bar graphs below showing the properties of the currents. (The kinetic values are time constants.) *pF*, picofarads. *B*, concentration-response curves for wild-type and CFP/YFP-tagged receptors. *C*, images of two HEK cells expressing P2X$_4$-CFP and P2X$_4$-YFP before and after photodestruction of the acceptor YFP. Note that the fluorescence intensity of the YFP channel decreases following photodestruction, whereas that of the CFP channel increases. The images were from the 30-min photodestruction time point. *D*, time course of YFP photodestruction and CFP photorecovery for whole-cell and near membrane regions. Graphs such as these are used to determine FRET *e*. YFP photodestruction is plotted *versus* CFP photorecovery, and the data are fit with a straight line and extrapolated to 100% YFP photodestruction. The intersection with the *y axis* represents the FRET *e* (see Fig. 3).

compared the responses with wild-type P2X receptors (Fig. 1). Receptor function was preserved for all receptors and the kinetics of their activation, desensitization, and deactivation were not detectably affected for some receptors. Below and in Fig. 2, we present a detailed characterization of these parameters for P2X$_4$ receptors. Thus, as expected (3), YFP-tagged P2X$_1$ and P2X$_3$ receptors desensitized rapidly (<1 s); P2X$_2$ and P2X$_4$ receptors desensitized slowly (over tens of seconds); and P2X$_5$ receptors expressed poorly (100 μM ATP used for activation). In the case of P2X$_7$ receptors, we recorded large variability in 30 μM benzoyl-ATP-evoked currents. Thus, in the case of the wild-type or YFP-tagged receptors, the currents from single cells were either monophasic or biphasic and displayed slow and variable kinetics (three exemplar traces are shown in Fig. 1). These cell-to-cell differences for P2X$_7$ receptors have been well documented and may represent permeability changes (33), variable phosphorylation (34), interactions with pannexin-1 channels (35, 36), or modulation by calmodulin (37). The focus of this study was not P2X$_7$ receptors, so we cannot yet discriminate between these possibilities. The key point here is that the wild-type and YFP-tagged P2X$_7$ receptors show similar overall responses, but in future work it will be important to determine the most critical factors that contribute to P2X$_7$ response variability. These overall features show that YFP tagging does not largely affect the functional properties of homomeric P2X receptors or peak currents (Fig. 1). We did not carry out an extensive pharmacological analysis of each tagged receptor because this was not the focus of this study and also because this has been reported already with GFP-tagged P2X$_2$, P2X$_4$, and P2X$_5$ receptors (15–25). Because the structure of CFP and YFP is similar to that of GFP and because they differ by only a few residues (32), it is reasonable to surmise that receptors that can be tagged with GFP can also tolerate CFP and YFP without altering function. Published data show this is the case for P2X$_2$ and P2X$_4$ receptors (15, 17, 18, 21, 23–25).

Functional Properties of CFP- and YFP-tagged P2X$_4$ Receptors—In the remainder of this study, we focused on homomeric P2X$_4$ receptors, and so we began by determining if CFP or YFP tagging affects the overall properties of P2X$_4$ receptors (Fig. 2, *A* and *B*). Fig. 2*A* shows average 100 μM ATP-evoked currents from cells expressing wild-type P2X$_4$, P2X$_4$-YFP, or P2X$_4$-CFP receptors. The traces are shown as picoamps/picofarads and clearly show that CFP or YFP tagging did not significantly affect the peak responses or the overall shape of the ATP-evoked current waveforms ($n = 9$). The bar graphs in Fig. 2*A* plot the average rise time (milliseconds), percent desensitization in 2 s of ATP, and decay time (milliseconds) after ATP removal for wild-type and CFP/YFP-tagged P2X$_4$ receptors. We next examined the ATP concentration dependence of the ATP-evoked responses for wild-type and CFP/YFP-tagged receptors. Fig. 2*B* shows that the concentration-response curves superimpose with EC$_{50}$ values of ~3 μM and Hill slopes of ~1.5 ($n = 8$). These values are similar to previous work on wild-type P2X$_4$ receptors (38). Overall, our data with CFP- and YFP-tagged receptors reproduce past work with GFP-tagged P2X$_4$ receptors, where it was demonstrated that GFP did not affect P2X$_4$ responses (15).

Receptor-specific FRET for Homomeric P2X Receptors—To measure FRET efficiency (*e*), we studied homomeric P2X receptors tagged with CFP and YFP and expressed in single living HEK cells. We focused on plasma membrane regions of interest and used donor dequenching (30) to estimate FRET *e* for P2X receptors in these regions (19, 39, 40). In Fig. 2 (*B* and *C*), we present representative images and graphs for P2X$_4$-CFP/P2X$_4$-YFP receptors. We measured a decrease in P2X$_4$-YFP fluorescence intensity with a time course that followed that of the P2X$_4$-CFP increase when the acceptor YFP was optically destroyed with 525 nm light (Fig. 2*C*). Maximum P2X$_4$-CFP photorecovery when P2X$_4$-YFP was 100% photodestroyed cor-

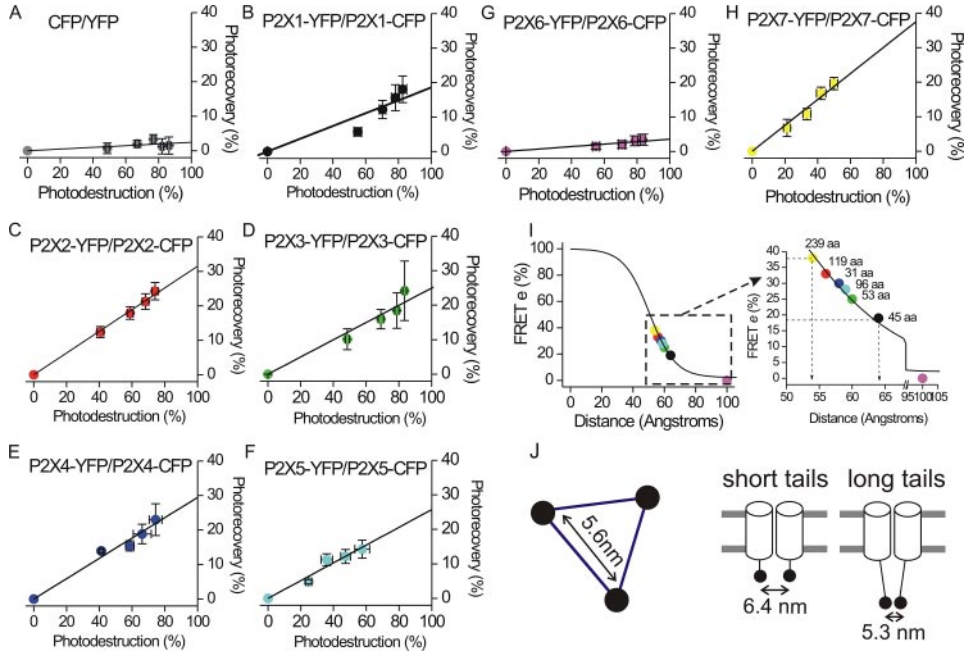

FIGURE 3. **FRET *e* for all homomeric P2X receptors for near membrane regions of interest and relationship of FRET *e* and interfluorophore distance.** *A–H*, in each case, linear plots of YFP photodestruction and CFP photorecovery are shown for the indicated constructs. In each case, FRET *e* is given by the *y axis* intercept of the straight line fits. The FRET *e* value from a linear fit to the mean data for CFP/YFP represents FRET noise. In the case of tagged P2X$_6$ receptors, only whole-cell regions were examined because these do not express in the plasma membrane, but are instead retained within intracellular membranes (see "Results"). *I*, the *left panel* shows a plot of the Förster equation relating FRET *e* (*y axis*) and interfluorophore distance (*x axis*), with FRET *e* data for all homomeric P2X receptors superimposed. The *boxed* region is expanded in the *right panel*. *J*, the *left panel* shows the measured distance between the C-terminal tails of P2X$_4$ monomers within the trimer (5.6 nm). The *right panel* summarizes the trend that was observed in the P2X receptor data, *viz.* that receptors with short C termini display lower FRET *e* values (thus, greater interfluorophore distance), and those with longer tails display higher FRET *e* values (thus, greater interfluorophore distance). In interpreting these data, it is important to remember that the orientation factor κ^2 is taken as 2/3 and assumes random tumbling as discussed by us and others (19, 30). *aa*, amino acids.

responds to FRET *e*, which in the case of P2X$_4$-CFP/P2X$_4$-YFP channels near the cell perimeter was 30 ± 5% (n = 8). We repeated these experiments to establish the level of FRET noise that arises as CFP and YFP randomly approach a distance of ~20–70 Å within the cell. The measured FRET efficiency for cytosolic CFP and YFP and P2X$_6$-CFP and P2X$_6$-YFP receptors within HEK cells was ~3% (Fig. 3*A*). In these experiments, we used P2X$_6$ receptors as a negative control because they do not express in the plasma membrane and are unassembled (41). We next extended the work by measuring FRET *e* for all homomeric P2X receptors in plasma membrane regions. The donor dequenching plots are presented in Fig. 3. These experiments clearly establish that FRET *e* for receptors in plasma membrane regions is subunit-specific. In the case of P2X$_6$ receptors, we could not measure FRET *e* for membrane regions because these channels are retained within the cell in intracellular compartments (41).

We explored the relationship of the experimentally determined FRET *e* for P2X receptors in the membrane to the dependence of FRET between CFP and YFP and interfluorophore distance (in angstroms). For this comparison, we used the Förster equation and an R_0 value of 50 Å. The graph in Fig. 3*I* plots FRET *e* for all homomeric P2X receptors along with how FRET *e* falls (as $1/R^6$) with distance between the chromophores of CFP and YFP. The numbers next to the data points indicate the length of the cytosolic C-terminal tail for each of the receptors. From these data, a trend is readily apparent. The FRET *e* for P2X receptors (and thus one assumes the interfluorophore distance) is related to the length of the C-terminal tail. For instance, the channels with the shortest C-terminal tails display the lowest FRET *e* (*e.g.* P2X$_1$ and P2X$_3$, C-terminal tail lengths of 44 and 42 residues), whereas the channels with the longest C-terminal tails display the highest FRET *e* (*e.g.* P2X$_2$ and P2X$_7$, C-terminal tail lengths of 118 and 238 residues). P2X$_5$ sits intermediate in this trend, consistent with its C-terminal tail being of intermediate length (96 residues). P2X$_4$ with a C-terminal tail length of 33 residues is the receptor that is slightly shifted in the overall trend. Overall, our data show a surprising trend between FRET *e* for P2X receptors and the C-terminal tail length, implying that the distance between the tips of the C-terminal tails for P2X receptors near the membrane is larger than at the tips of those with longer tails. Put another way, the cytosolic domain of P2X$_2$ and P2X$_7$ receptors narrows from its origins at the plasma membrane to its tip (Fig. 3*J*). Using this method, the distance between the C-terminal tails of functional P2X$_4$ receptors in the plasma membrane of single living cells was calculated to be 5.6 nm.

All of the FRET experiments shown in Fig. 3 were carried out using identical imaging/analysis methods and in parallel to reduce any variability between experiments. In the case of P2X$_2$–P2X$_6$ receptors, the data points were well fit by a straight line (Fig. 3). However, in the case of P2X$_1$ and P2X$_7$ receptors, the linear plots were less esthetically pleasing. We could think of no precise scientific reason to discard these data and present them faithfully in Fig. 3. The relevant issue here is whether the FRET *e* estimates for P2X$_1$ and P2X$_7$ receptors were adversely affected. To address this, we specifically determined if estimates of FRET *e* were adversely affected by prolonged photodestruction that is needed for the linear plots in Fig. 3. We measured FRET *e* for all homomeric P2X receptors from only one point of photodestruction and compared the estimated FRET *e* values with those determined with extensive photodestruction (Fig. 2, *C* and *D*, and Fig. 3). Fig. 4 shows that FRET values agree between these methods. Thus, although there is some variability between P2X receptors in the extent to which the CFP photorecovery is fit by linear functions (compare plots in Fig. 3), this does not under- or overestimate FRET *e* values. This is consistent with past work for a variety of FRET constructs, including P2X$_2$ receptors, where we showed using three-cube

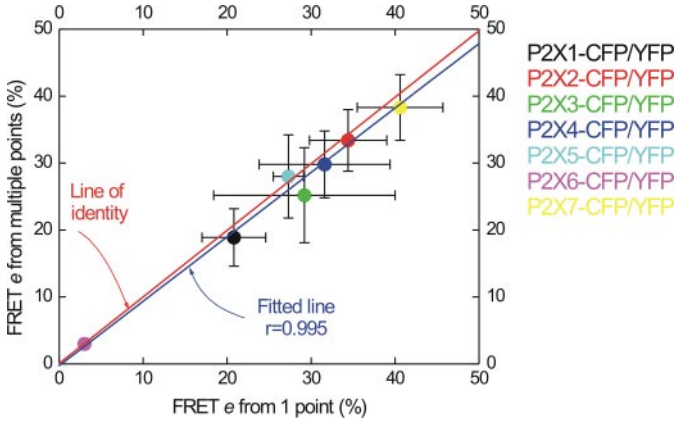

FIGURE 4. **Comparison of P2X receptor FRET by two methods.** The graph shows the relationship between FRET *e* estimates from experiments such as those in Fig. 3 when extensive photobleaching was employed (~30 min) and FRET *e* estimates when only 5 min of photodestruction was used. The graph shows strong agreement in FRET *e* values for these two donor dequenching methods (see "Results" for further details).

linear unmixing that FRET *e* could be reliably estimated by donor dequenching (Figs. 3 and 4) (18).

We next sought to generate a three-dimensional structure of purified human P2X$_4$ protein. Our reasoning was 2-fold. First, because FRET is an ensemble measurement and makes a number of assumptions about the fluorophore orientations, a three-dimensional structure could be used to verify the FRET *e* measurements. Second, the estimates of distance by FRET may be used as a "barometer" to ascertain that the P2X$_4$ structure was of a size appropriate for the channel in the membrane. This is important because the published single particle and AFM studies differ largely on the dimensions of P2X receptors (see the Introduction).

Functional Expression and Purification of Human P2X$_4$-His$_{10}$ from HEK Cells—The expression of human P2X$_4$-His$_{10}$ was verified by Western blotting and compared with that of P2X$_4$-EYMPME (26). Both the C-terminal P2X$_4$ epitope and the His tag were readily detected, and total protein expression levels appeared to be similar to those of P2X$_4$-EYMPME (data not shown). Whole-cell currents were evoked by a 2-s application of 1, 10, and 100 μM ATP in perforated patch-clamp configuration; peak current densities to 100 μM ATP were 40 ± 4 pA/picofarads for P2X$_4$-EYMPME and 45 ± 6 pA/picofarads for P2X$_4$-His$_{10}$ (n = 8). EC$_{50}$ values were 2.9 ± 0.2 μM for P2X$_4$-EYMPME and 2.7 ± 0.3 μM for P2X$_4$-His$_{10}$ (n = 8).

Following nickel affinity chromatography, the majority of P2X$_4$ eluted in the 500 mM imidazole fraction as a diffuse 55-kDa band. The size of the band was in agreement with that observed by Western blotting, and purity was estimated to be ~50%. To purify P2X$_4$ to homogeneity, we used nondenaturing PFO-PAGE (28), followed by electroelution. When separated by PFO-PAGE, 50% pure P2X$_4$ presented as three bands corresponding to a monomer (55 kDa), a faint dimer (110 kDa), and a trimer (165 kDa) (Fig. 5*A*). No higher order oligomers were observed. We assumed that the observed monomers and dimers corresponded to immature nonassembled proteins recovered from internal membranes. Trimers were selectively purified by excising bands from preparative nonstained PFO-polyacrylamide gels and eluting protein under an electric field.

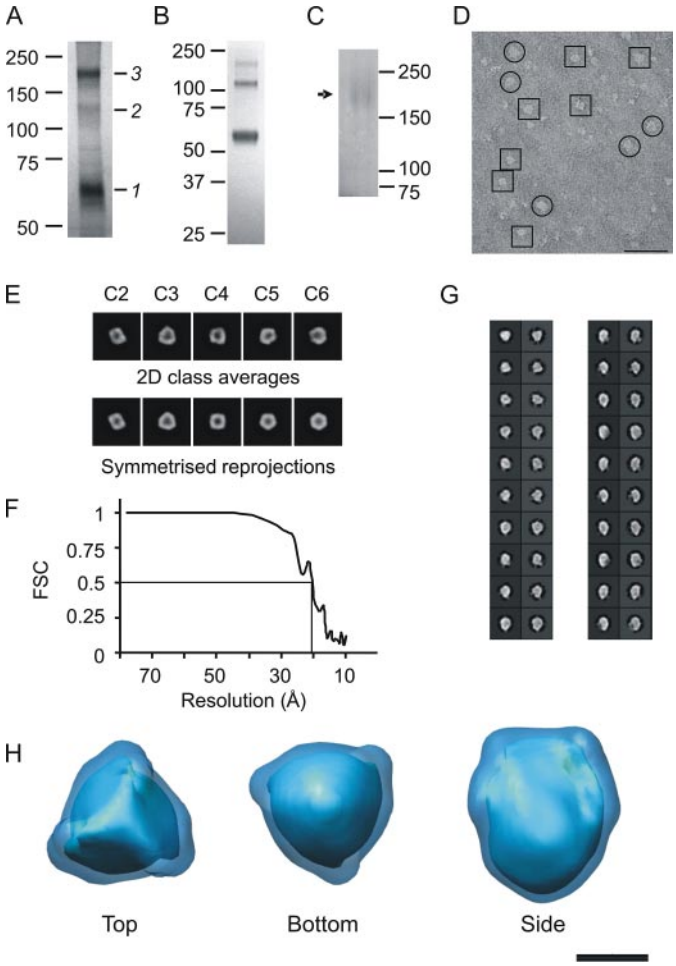

FIGURE 5. **Purification and 21 Å structure of P2X$_4$ receptor trimers.** *A*, Coomassie Blue-stained 8% (w/v) PFO-polyacrylamide gel of partially purified P2X$_4$ after nickel chromatography. The molecular masses of monomer (55 kDa), dimer (110 kDa), and trimer (165 kDa) bands are indicated (*1*, *2*, and *3* respectively). *B*, silver-stained SDS-polyacrylamide gel of purified human P2X$_4$ trimers following gel excision and electroelution. A high purity was obtained; SDS-stable dimeric and trimeric forms of protein are also visible. *C*, silver-stained PFO-polyacrylamide gel of purified trimers demonstrating that the trimeric form was stable after purification (indicated by the *arrow*). *D*, particle field from an electron micrograph of negatively stained (2% (w/v) uranyl acetate) single particles of human P2X$_4$-His$_{10}$. Single particles are indicated by 48 × 48 pixel square *boxes* (top/bottom views) and 48 pixel radius *circles* (side views). *E*, symmetry analysis of two-dimensional reference-free class averages using the command startcsym at C2, C3, C4, C5, and C6 symmetry. The best fitting class average is displayed above the corresponding symmetrized view (sym); C3 symmetry produces the best fit with the class average. *F*, Fourier shell correlation (*FSC*) analysis of structures of wild-type human P2X$_4$ generated from even- and odd-numbered particles using the command eotest. The resolution of the structure given by the Fourier shell correlation value of 0.5 is indicated and corresponds to ~21 Å. *G*, class averages generated by single particle analysis of the wild-type particle data set. Each *column* represents a back-projection from the final C3-symmetrized three-dimensional volume paired with its corresponding unsymmetrized class average. A selected range of views from top/bottom (*top left column*) to side (*bottom right column*) are displayed. *Box* size is 234 × 234 Å. *H*, structure of human P2X$_4$ at 21 Å resolution displayed at two volume thresholds (5.6σ, *light blue inner core*; and 3σ, *dark blue outer shell*) above the mean density. *Scale bar* = 50 Å.

SDS-PAGE analysis of eluted protein demonstrated the high purity obtained using this purification method (Fig. 5*B*); the only bands visible on the silver-stained gel corresponded to P2X$_4$. (SDS-stable dimeric and trimeric forms were also observed.) In addition, PFO-PAGE of purified trimers was used to demonstrate that the trimeric form was stable after purifica-

tion (Fig. 5*C*, *arrow*). After diafiltration into 0.1% (w/v) DDM, 40 μl of $P2X_4$ was recovered at an approximate concentration of 1 mg/ml. Yield was estimated by comparing the band intensity of pure $P2X_4$ on Coomassie Blue-stained SDS-polyacrylamide gels with known quantities of bovine serum albumin. In summary, 40 μg of pure $P2X_4$ trimer was recovered from 2.5×10^8 cells (equivalent to a confluent monolayer of 5000 cm^2 in area).

Electron Microscopy and Single Particle Analysis—Pure protein was diluted to 25 μg/ml, applied to electron microscopic (EM) grids, and negatively stained with 2% (w/v) uranyl acetate. An image field for wild-type human $P2X_4$ is shown in Fig. 5*D*. Single particles of the $P2X_4$ receptor were relatively homogeneous, with the majority (~70%) appearing either nearly circular, with a radius of ~8 nm, or nearly rectangular, with a short side of 8 nm and a long side of 12 nm. We interpreted these particles as either top/bottom views or side views, respectively. In total, 6826 particles were manually selected in 48×48 pixel boxes for image processing using the EMAN software package (29). Reprojections of the C3-symmetrized three-dimensional structure, paired with their corresponding unsymmetrized class averages, are shown in Fig. 5*G*. Representations of the structure of human $P2X_4$ were generated and are shown in Fig. 5*H*. The resolution of the wild-type structure was ~21 Å as judged by Fourier shell correlation of structures calculated from sets of even- and odd-numbered particles (Fig. 5*F*).

Gold and Lectin Labeling—To orient our structure, the C-terminal His tags of human $P2X_4$ were labeled using 1.8-nm diameter Ni-NTA-Nanogold particles and washing our EM grids in a Nanogold suspension to prevent unbinding during sample preparation. A high off-rate for this probe has recently been described (42). We selected 1966 particles with at least one gold particle attached. A sample field of view is displayed in Fig. 6*A*. Reprojections of the C3-symmetrized three-dimensional structure, paired with their corresponding unsymmetrized class averages, are shown in Fig. 6*C*. Gold particles were clearly visible, with some classes containing two attached gold particles per trimer. The gold-labeled particles were significantly smaller than the wild-type particles, most noticeably in areas near where the gold was bound, due to the strong negative density of the gold overshadowing the protein density within its vicinity.

The extensive glycosylation present on human $P2X_4$ receptors enabled labeling of the ectodomain with *L. culinaris* lectin at a 1:1 molar ratio. Analyzed by transmission electron microscopy, the single particles were heterogeneous (Fig. 6*B*), which was expected considering the potential number of lectin-binding sites per $P2X_4$ molecule. 2862 particles were manually selected in 64×64 pixel boxes, and reprojections of the C3-symmetrized three-dimensional structure, paired with their corresponding unsymmetrized class averages, are shown in Fig. 6*D*.

Three-dimensional Structure of Human $P2X_4$ at 21 Å Resolution—The overall shape of the molecule was globular and somewhat reminiscent of a torpedo (Fig. 5*H*); in the gold-labeled structure, three strong negative densities corresponding to the 1.8-nm diameter gold spheres were clearly averaged into the density map toward the narrow end of the molecule (Fig. 6*E*), implying that the propeller-like structure at the top of the molecule corresponded to the ectodomain. The distance between the centers of the gold particles was 6.1 nm (Fig. 6*E*, *black arrow*), which agrees well with the data from FRET experiments (5.6 nm) (Fig. 6*E*, *red arrow*). In confirmation that we had assigned the correct orientation, the lectin-labeled particle clearly displayed two regions of additional protein density per monomer at the propeller end of the molecule (Fig. 6*F*). The molecular mass of *L. culinaris* lectin tetramers is 49 kDa, but the additional volume observed in the labeled structure was smaller than expected for three tetramers. This is probably because lectin bound to $P2X_4$ *N*-linked glycan chains present at different positions in the ectodomain, and furthermore, flexibility of each glycan chain could also lead to a smearing out of the lectin location. Such variability would lead to some averaging out of the lectin location by single particle analysis so that only the core of the lectin binding to $P2X_4$ would be observed in the final structure.

At a threshold of 5.6σ above the mean density (Fig. 5*H*, *light blue inner core*), the human $P2X_4$ receptor ectodomain displayed cavities with lateral fins running alongside them. This volume threshold corresponds to a molecular mass of 220 kDa and a volume of 270 nm^3, allowing for one $P2X_4$ trimer in addition to a detergent micelle (assuming a protein density of 1.35 g/ml and no significant internal cavities within the structure). At 3σ above the mean density (Fig. 5*H*, *dark blue outer core*), the cavities disappeared, and the lateral fins were more pronounced. This density corresponds to a molecular mass of 410 kDa and a volume of 506 nm^3. Our value for the molecular volume of human $P2X_4$ of 270 nm^3 is consistent with the value of 409 nm^3 obtained for rat $P2X_2$ using AFM imaging (trimer masses of 165 kDa for human $P2X_4$ and 210 kDa for rat $P2X_2$) (10). The transmembrane domains are most likely shrouded in a torus-shaped detergent micelle, which could explain the bulbous nature of the $P2X_4$ three-dimensional structure in the region below the fins that we associate with the ectodomain. However, we cannot rule out the possibility that regions of the ectodomain re-enter the transmembrane region and contribute to the protein content of the transmembrane space.

DISCUSSION

The main results of this study are (*i*) we developed methods to overexpress $P2X_4$ receptors for structural work; (*ii*) we determined the shape, architecture, and size of a single human P2X receptor; and (*iii*) we verified the dimensions with independent measurements using FRET. We initially chose to work on all homomeric P2X receptors using FRET microscopy and measured the proximity between their C-terminal tail tips at 5.3–6.4 nm. We then focused on $P2X_4$ receptors for electron microscopy because of its favorable expression profile (43). The single particle studies provide data on the overall shape and size of a single P2X receptor and on the approximate distance between the C-terminal tail tips at 6.1 nm. The agreement for proximity between FRET and electron microscopy attests to the reliability of the methods. Förster theory of energy transfer makes several assumptions about the mutual orientation of the fluorophores (notably the κ^2 value). In the usual case, κ^2 is taken to equal 2/3, which implies adoption of all spherically random orientations

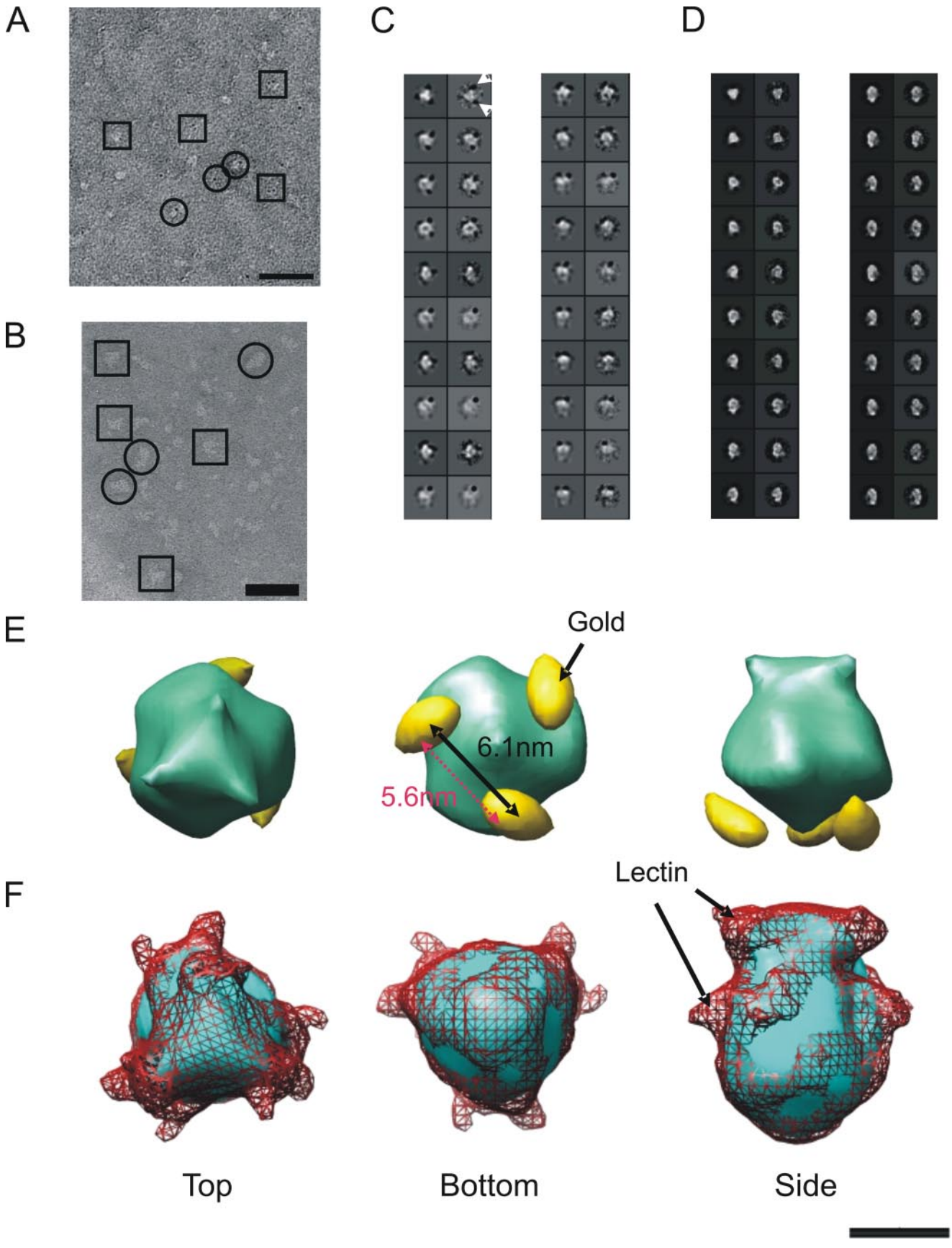
A
B
C
D
E
Gold
6.1nm
5.6nm
F
Lectin
Top
Bottom
Side

between the fluorophores (30). The agreement for distance estimates by FRET and single particle imaging suggests that FRET is useful as a molecular caliper for membrane-embedded P2X channels. This is consistent with previous pioneering FRET studies by Nashmi *et al.* (39) of neuronal nicotinic receptors and comparisons of distance to the structural model of the muscle nicotinic receptor (19, 39, 40).

One of the key issues in the P2X field is the need to obtain direct structural information for this novel class of membrane proteins. This is a nontrivial issue because no P2X receptors have been found in bacteria, and there are no other receptors with similar structure based on sequence analysis. This calls for the development of approaches that can be used for the expression and purification of P2X receptors. In this work, we have both developed an efficient expression and purification system for human P2X$_4$ and significantly improved the quality and resolution of existing structural data available for P2X receptors. Our methods should also enable relatively straightforward purification of larger quantities of human P2X$_4$ for higher resolution structure studies. Preparative electrophoresis has been used extensively for the purification of membrane protein complexes (44), and in at least one case, this method has yielded sufficient quantities for three-dimensional crystallization (45). The use of our method, by us and others, will allow high resolution structural information on P2X receptors.

Selective purification by preparative electrophoresis of a band corresponding in apparent molecular mass to a trimeric form of human P2X$_4$ strongly suggested the application of C3 symmetry in image processing and three-dimensional reconstruction. Since initial pioneering work with Blue native PAGE by Nicke *et al.* (8), virtually all recent evidence also indicates that trimers are the functional unit of P2X receptors (9–11). In addition, we were able to label the C-terminal His tags on each monomer with 1.8-nm gold particles. Although three gold particles attached to a single trimeric particle were only infrequently observed, probably because of a relatively weak binding or a rapid off-rate (42), many particles were doubly labeled, and after classification and averaging, a 120° angle was subtended between the two gold labels in the classes corresponding to "face-on" views along the C3 axis of rotational symmetry (Fig. 6*C*, *arrows*).

Labeling of the large, multiply glycosylated ectodomain with plant lectin confirmed that the "propeller"-like domain, previously identified in the low resolution structural analysis as being at the opposite end of the molecule to the Ni-NTA-gold label, probably corresponded to this extracellular region. A composite model based on all the EM data is shown in Fig. 5.

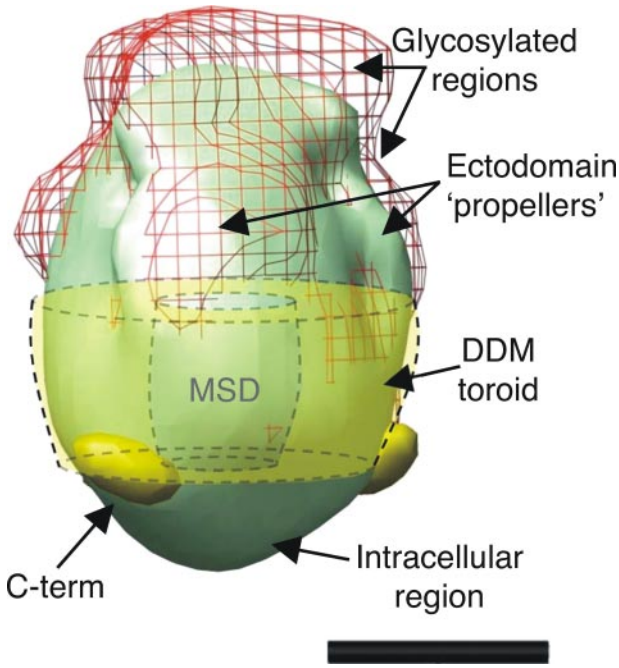

FIGURE 7. **Model of human P2X$_4$ receptor based on EM data.** The side view of the structure of wild-type human P2X$_4$ is shown in *light green* (intracellular region at the bottom). Additional density imparted by the lectin labeling, assumed to be regions of glycosylation on the ectodomain, is shown as a *dark pink mesh*, and the gold particles marking the position of the C termini (*C-term*) are also displayed toward the bottom of the molecule. The approximate position of a toroidal DDM micelle surrounding the membrane-spanning domain (*MSD*) is also included in the model. *Scale bar* = 50 Å.

Note that the expected dimensions of a torus-shaped DDM micelle are indicated, which would leave a relatively small volume at its center corresponding to the transmembrane regions of P2X$_4$. The final structure is therefore expected to be torpedo-shaped, with a narrow transmembrane domain and compact ectodomain that does not display a central cavity or pore. Approximate maximum dimensions were 8 nm in diameter and 12 nm along the longest axis, coincident with the C3 symmetry axis. Under our experimental conditions, in which P2X$_4$ was solubilized in detergent, the position of the membrane-spanning domain could not be accurately determined; however, we have indicated its approximate position in Fig. 7. It is probable that the transmembrane domains were protected from the aqueous environment by a detergent micelle, which could possess a molecular mass of in excess of 50 kDa. However, our structure does not inform us about protein organization within the transmembrane region, and it is possible that regions of the ectodomain may form re-entrant loops, increasing the protein

FIGURE 6. **Domain-specific labeling of P2X$_4$ receptor trimers.** *A*, particle field from an electron micrograph of negatively stained (2% (w/v) uranyl acetate) single particles of human P2X$_4$-His$_{10}$ following a 10-min incubation with 1.8-nm diameter Ni-NTA-Nanogold particles. Single particles are indicated by 48 × 48 pixel square *boxes* (top/bottom views) and 48 pixel radius *circles* (side views). *B*, particle field of human P2X$_4$ following incubation with a 1:1 molar ratio of *L. culinaris* lectin. Single particles are indicated by 64 × 64 pixel square *boxes* (top/bottom views) and 64 pixel radius *circles* (side views). Significant heterogeneity of the particles may be observed. *C* and *D*, class averages generated by single particle analysis of gold-labeled (*C*) and lectin-labeled (*D*) particle data sets. Each *column* represents a back-projection from the final C3-symmetrized three-dimensional volume paired with its corresponding unsymmetrized class average. A selected range of views from top/bottom (*top left column*) to side (*bottom left column*) are displayed. The location of gold particles in the unsymmetrized class averages is indicated by the *white arrowheads* in the first box (*C*). Box sizes are 234 × 234 Å for the gold-labeled data set and 312 × 312 Å for the lectin-labeled data set. *E*, top, bottom, and side views of gold-labeled P2X$_4$ showing the position of the C-terminally attached gold particles. The distance between the centers of the gold particles (indicated by the *black arrow*) was 6.1 nm. The *red arrow* indicates the distance between fluorophores observed in FRET experiments. *F*, top, bottom, and side views of lectin-labeled P2X$_4$ showing the small regions of additional density imparted by lectin binding to the ectodomain. *Scale bars* = 50 Å.

content within the transmembrane space. In the model shown in Fig. 7, the C-terminal decahistidine tag is positioned close to the start of the membrane-spanning domain, a location that would place it close to the polar headgroup region of the inner leaflet of the plasma membrane.

Our work represents the first direct structural study of a human P2X receptor, but should be discussed in the light of previous work on rat $P2X_2$. Mio *et al.* (13) purified rat $P2X_2$ from an insect cell line and determined a structure by transmission electron microscopy and single particle analysis. Their structure resembled an inverted three-sided pyramid, 21.5 nm in height and 20 nm in side length, corresponding to a molecular volume of ~1200 nm^3; this is 4.5-fold greater than our measurement of 270 nm^3. The authors stated that their model contained a large, stain-permeable cavity; however, as the orientation of the particle was not assigned, it was not possible to state which portion of the molecule contained the cavity in their experiments. The authors assumed that this portion of their structure corresponded to the ectodomain by comparison with the topology map of the receptor. However, our data clearly show that the ectodomain of human $P2X_4$ is a highly compact structure, such as has been shown in the recently published structure of the trimeric acid-sensing ion channel 1 (12). Given the high degree of sequence homology between rat $P2X_2$ and human $P2X_4$, it seems unlikely that the structures at the monomeric level would be so radically different in size and shape. A possible explanation for the discrepancy may be that the rat $P2X_2$ particles were composed of a higher order quaternary structure. Four trimeric $P2X_2$ complexes of the dimensions described here could potentially associate into a large complex with tetragonal symmetry. Such a tetramer of trimers, composed of 12 $P2X_2$ polypeptides, would account for the ~4-fold greater volume of the rat $P2X_2$ particles *versus* expectations and the very large (20-nm side length) overall dimensions of the pyramidal particles. Two additional studies of rat $P2X_2$ structure have been published. Nakazawa *et al.* (14) analyzed single particles of rat $P2X_2$ using AFM. They found that in the presence of 1 mM ATP, particles of ~10 nm in diameter were observed, with evidence suggesting the presence of a central pore. The diameter of these particles is more consistent with those observed for human $P2X_4$ in our study (8-nm diameter along the C3 axis); however, at the resolution of our study, we could not observe a central pore. It is possible that AFM, which measures the surface topography of the specimen, is detecting an indentation in $P2X_2$ that is not present in $P2X_4$ or, alternatively, that the negative staining and EM method do not access this surface topography in $P2X_4$. Barrera *et al.* (10) also imaged rat $P2X_2$ using AFM. They provided evidence for the trimeric nature of rat $P2X_2$ by measuring the average angle (120°) between peripheral particles interpreted as antibodies attached to the (three) C termini of their $P2X_2$ specimen. Their estimate of the volume of the receptor was 409 nm^3, which is consistent with our measurement for human $P2X_4$ of 270 nm^3, allowing for the difference in molecular mass between the two receptor subtypes (165 kDa for human $P2X_4$ trimers *versus* 210 kDa for rat $P2X_2$ trimers).

In summary, we have introduced an efficient method for purification of human $P2X_4$ that has been overexpressed in human cells. This methodology may be readily applicable to other members of this family and could be of interest for the purification of other membrane proteins where isolation of a single oligomeric form is desirable. This method has allowed us to study the overall structure and topology of $P2X_4$ and has helped to interpret existing structural data for this unique and intriguing family of nonselective cation channels. Our work has enabled visualization of some global structural features of these receptors and paves the way for future studies. This work should be viewed as an initial and necessary step toward the longer term goal of obtaining high resolution structural information for P2X receptors. From this perspective, it is worth considering that spectacular progress has been made using cryoelectron microscopy studies of nicotinic receptors since initial views of the quaternary structure published in 1985 (46) to a recent 4 Å resolution model (47).

Acknowledgments—We thank Helen Broomhead for assistance with molecular biology and Kyriaki Dossi and Joan Sim for assistance with cell culture.

REFERENCES

1. Burnstock, G. (2007) *Physiol. Rev.* **87,** 659–797
2. Khakh, B. S., and North, R. A. (2006) *Nature* **442,** 527–532
3. North, R. A. (2002) *Physiol. Rev.* **82,** 1013–1067
4. Fountain, S. J., Parkinson, K., Young, M. T., Cao, L., Thompson, C. R., and North, R. A. (2007) *Nature* **448,** 200–203
5. Lester, H. A., Dibas, M. I., Dahan, D. S., Leite, J. F., and Dougherty, D. A. (2004) *Trends Neurosci.* **27,** 329–336
6. Mayer, M. L., and Armstrong, N. (2004) *Annu. Rev. Physiol.* **66,** 161–181
7. Sine, S. M., and Engel, A. G. (2006) *Nature* **440,** 448–455
8. Nicke, A., Baumert, H. G., Rettinger, J., Eichele, A., Lambrecht, G., Mutschler, E., and Schmalzing, G. (1998) *EMBO J.* **17,** 3016–3028
9. Aschrafi, A., Sadtler, S., Niculescu, C., Rettinger, J., and Schmalzing, G. (2004) *J. Mol. Biol.* **342,** 333–343
10. Barrera, N. P., Ormond, S. J., Henderson, R. M., Murrell-Lagnado, R. D., and Edwardson, J. M. (2005) *J. Biol. Chem.* **280,** 10759–10765
11. Jiang, L. H., Kim, M., Spelta, V., Bo, X., Surprenant, A., and North, R. A. (2003) *J. Neurosci.* **23,** 8903–8910
12. Jasti, J., Furukawa, H., Gonzales, E. B., and Gouaux, E. (2007) *Nature* **449,** 316–323
13. Mio, K., Kubo, Y., Ogura, T., Yamamoto, T., and Sato, C. (2005) *Biochem. Biophys. Res. Commun.* **337,** 998–1005
14. Nakazawa, K., Yamakoshi, Y., Tsuchiya, T., and Ohno, Y. (2005) *Eur. J. Pharmacol.* **518,** 107–110
15. Yan, Z., Liang, Z., Tomic, M., Obsil, T., and Stojilkovic, S. S. (2005) *Mol. Pharmacol.* **67,** 1078–1088
16. Bo, X., Jiang, L. H., Wilson, H. L., Kim, M., Burnstock, G., Surprenant, A., and North, R. A. (2003) *Mol. Pharmacol.* **63,** 1407–1416
17. Bobanovic, L. K., Royle, S. J., and Murrell-Lagnado, R. D. (2002) *J. Neurosci.* **22,** 4814–4824
18. Fisher, J. A., Girdler, G., and Khakh, B. S. (2004) *J. Neurosci.* **24,** 10475–10487
19. Khakh, B. S., Fisher, J. A., Nashmi, R., Bowser, D. N., and Lester, H. A. (2005) *J. Neurosci.* **20,** 6911–6920
20. Khakh, B. S., and Egan, T. M. (2005) *J. Biol. Chem.* **280,** 6118–6129
21. Khakh, B. S., Smith, W. B., Chiu, C. S., Ju, D., Davidson, N., and Lester, H. A. (2001) *Proc. Natl. Acad. Sci. U. S. A.* **98,** 5288–5293
22. Richler, E., Chaumont, S., Shigetomi, E., Sagasti, A., and Khakh, B. S. (2008) *Nat. Methods* **5,** 87–93
23. Royle, S. J., Bobanovic, L. K., and Murrell-Lagnado, R. D. (2002) *J. Biol. Chem.* **277,** 35378–35385
24. Royle, S. J., Qureshi, O. S., Bobanovic, L. K., Evans, P. R., Owen, D. J., and

Murrell-Lagnado, R. D. (2005) *J. Cell Sci.* **118,** 3073–3080
25. Samways, D. S., and Egan, T. M. (2007) *J. Gen. Physiol.* **129,** 245–256
26. Fountain, S. J., and North, R. A. (2006) *J. Biol. Chem.* **281,** 15044–15049
27. Egan, T. M., Haines, W. R., and Voigt, M. M. (1998) *J. Neurosci.* **18,** 2350–2359
28. Ramjeesingh, M., Huan, L. J., Garami, E., and Bear, C. E. (1999) *Biochem. J.* **342,** 119–123
29. Ludtke, S. J., Baldwin, P. R., and Chiu, W. (1999) *J. Struct. Biol.* **128,** 82–97
30. Michalet, X., Kapanidis, A. N., Laurence, T., Pinaud, F., Doose, S., Pflughoefft, M., and Weiss, S. (2003) *Annu. Rev. Biophys. Biomol. Struct.* **32,** 161–182
31. Bunt, G., and Wouters, F. S. (2004) *Int. Rev. Cytol.* **237,** 205–277
32. Tsien, R. Y. (1998) *Annu. Rev. Biochem.* **67,** 509–544
33. Surprenant, A., Rassendren, F., Kawashima, E., North, R. A., and Buell, G. (1996) *Science* **272,** 735–738
34. Kim, M., Jiang, L. H., Wilson, H. L., North, R. A., and Surprenant, A. (2001) *EMBO J.* **20,** 6347–6358
35. Pelegrin, P., and Surprenant, A. (2006) *EMBO J.* **25,** 5071–5082
36. Pelegrin, P., and Surprenant, A. (2007) *J. Biol. Chem.* **282,** 2386–2394
37. Roger, S., Pelegrin, P., and Surprenant, A. (2008) *J. Neurosci.* **28,** 6393–6401
38. Khakh, B. S., Burnstock, G., Kennedy, C., King, B. F., North, R. A., Séguéla, P., Voigt, M., and Humphrey, P. P. A. (2001) *Pharmacol. Rev.* **53,** 107–118
39. Nashmi, R., Dickinson, M. E., McKinney, S., Jareb, M., Labarca, C., Fraser, S. E., and Lester, H. A. (2003) *J. Neurosci.* **23,** 11554–11567
40. Drenan, R. M., Nashmi, R., Imoukhuede, P., Just, H., McKinney, S., and Lester, H. A. (2008) *Mol. Pharmacol.* **73,** 27–41
41. Le, K. T., Babinski, K., and Séguéla, P. (1998) *J. Neurosci.* **18,** 7152–7159
42. Lata, S., Gavutis, M., Tampé, R., and Piehler, J. (2006) *J. Am. Chem. Soc.* **128,** 2365–2372
43. Kawate, T., and Gouaux, E. (2006) *Structure* **14,** 673–681
44. Kashino, Y. (2003) *J. Chromatogr. B. Anal. Technol. Biomed. Life Sci.* **797,** 191–216
45. Ford, R. C., Picot, D., and Garavito, R. M. (1987) *EMBO J.* **6,** 1581–1586
46. Brisson, A., and Unwin, P. N. (1985) *Nature* **315,** 474–477
47. Unwin, N. (2005) *J. Mol. Biol.* **346,** 967–989